Evaluation of residual stress of *c* oriented AlN/Si (111) and its impact on mushroom-shaped piezoelectric resonator

Akhilesh Pandey[1,*] ⓘ, Shankar Dutta[1], Nidhi Gupta[1], Davinder Kaur[2], and R. Raman[1]

[1] *Solid State Physics Laboratory, DRDO, Lucknow Road, Timarpur, Delhi 110054, India*
[2] *Department of Physics, Indian Institute of Technology Roorkee, Roorkee 247667, India*

ABSTRACT

Aluminium nitride-based MEMS resonators are one of the interesting recent research topics for its tremendous potential in a wide variety of applications. This paper focuses on the detrimental effect of residual stress on the AlN-based MEMS resonator design for acoustic applications. The residual stress in the sputtered *c*-axis ($< 001 >$) preferred oriented AlN layers on Si (111) substrates are studied as a function of layer thickness. The films exhibited compressive residual stresses at different thickness values: $- 1050$ MPa (700 nm), $- 500$ MPa (900 nm), and $- 230$ MPa (1200 nm) with ± 25 MPa accuracy. A mushroom-shaped AlN-based piezoelectric MEMS resonator structure has been designed for the different AlN layer thicknesses. The effect of the residual stresses on the mode shapes, resonant frequencies, and quality factor (Q) of the resonator structures are studied. The resonant frequency of the structures are altered from 235 kHz, 280 kHz, and 344 kHz to 65 kHz, 75 kHz and 371 kHz due to the residual stress of $- 1050$ MPa (thickness: 700 nm), $- 500$ MPa (thickness: 900 nm) and $- 230$ MPa (thickness: 1200 nm), respectively. At no residual stress, the quality factors of the resonator structures are 248, 227, 241 corresponding to the 700 nm, 900 nm, and 1200-nm-thick AlN layers, respectively. The presence of the residual stress reduced the Q values from 248 (thickness: 700 nm), 227 (thickness: 900 nm), 241 (thickness: 1200 nm) to 28, 53, and 261, respectively.

Address correspondence to E-mail: akhilesh.physics@gmail.com

🍀 Springer

1 Introduction

Micro-electro-mechanical system (MEMS)-based sensors and actuators are used in a wide variety of applications such as military, aerospace, industrial, consumer electronics, healthcare, as well as in agriculture and environment monitoring [1–10]. The devices such as pressure sensors, accelerometers, gyroscope, and temperature sensors are the few most sort after MEMS sensors for these applications [8, 11–15]. On the other hand, smart actuation mechanisms such as shape-memory effect, electrostatic, magnetic and piezoelectric are intelligently employed to perform the various desired microscopic operation with great precision [7, 14, 16–20] Ever since the introduction of the famous mechanical resonator gate transistor reported by Nathan et al. [21], micro-resonators are the important building block of many MEMS devices [22–29]. Today, MEMS-based resonators have been used in oscillators [5], filters [16], gyroscope [11], micro-speaker [30], etc. The MEMS-based resonators are capable of sensing a very small change in mass loading thus having great potential in chemical and biomedical applications [27, 29].

Though PZT is one of the most widely studied piezoelectric MEMS material [6, 7, 30–32], AlN-based MEMS resonators on piezoelectric operating principle are found interests among the research community in recent time [5, 22–24, 28, 29]. Despite having lower piezoelectric coefficient than PZT, the choice of the AlN is driven by three major factors: (i) excellent thermal and chemical stability [33, 34]; (ii) excellent CMOS process compatibility [26]; and (iii) environment-friendly nature [35, 36].

Among different MEMS materials, silicon is widely used in MEMS technology because of its excellent mechanical properties, ease of micromachining, relatively low-cost [11, 14, 15, 35, 37, 38]. Thus, for the fabrication of AlN-based MEMS resonator structure, the integration of AlN layers on Si substrates is essential. The integration of AlN layers on Si substrate can have zinc-blend or wurtzite crystalline structure [35, 36, 38, 39]. The AlN thin film with < 001 > oriented (c-axis) wurtzite phase is preferred to enhance the piezoelectric effect [17, 33, 36]. Different deposition techniques are used to grow AlN layers on Si substrates such as atomic layer deposition [40], chemical vapour deposition [41], molecular beam epitaxy [42], pulsed laser deposition [43], and

sputtering [35, 36, 44, 45]. For MEMS device development, the Si (100) and Si (110) substrates are preferred because of their ease of micromachining in alkaline solutions (KOH, TMAH, NaOH, etc.). However, these substrate surfaces possess non-hexagonal arrangement of atoms which is not very favourable to grow c-axis oriented wurtzite AlN films. Thus growing the c-axis oriented AlN layers on the Si (100) and (110) substrate will add-up a high level of residual stress [35–45]. With the increasing use of sophisticated micromachining techniques like the deep reactive ion etching (DRIE) technique, it is possible to fabricate Si (111)-based bulk-micromachined devices [46]. The advantage of Si (111) substrate for the AlN-based piezoelectric MEMS devices is the hexagonal lattice arrangement of surface atoms, which favours < 001 > oriented AlN layer growth with minimum residual stress [45].

In the MEMS device front, Li et al. (2017) have designed and fabricated AlN-based piezoelectric-on-silicon low phase noise oscillator [5]. Alcheikh et al. (2018) investigated the performance of compound MEMS resonators with multiple inputs (actuation) and output (detection) methods [22]. Pfusterschmied et al. [9, 10] applied the piezoelectric MEMS resonators for grape must fermentation monitoring in 2017, and also studied the behaviour of piezoelectric MEMS resonators submerged in different liquids in 2019. Toledo et al. [28] demonstrated the potential of a piezoelectric resonator for developing a low-cost sensor system for the detection of microscopic particles present in environments and workplaces. Bao et al. [23] successfully implemented AlN-based SOI MEMS resonators having improved quality factor (Q factor). The team also (Bao et al. [24]) presented AlN-based high-Q multi-frequency ring-shaped piezoelectric MEMS resonators. However, any of the above research articles have not discussed the effect of residual stress in AlN layers on Si (111) substrate with the varying thickness on the performance of the MEMS resonator structure.

This paper discusses about the growth of c-axis preferred oriented AlN films on Si (111) substrates using the reactive DC sputtering technique. The phase, crystalline-quality, and morphology of the sputtered layers are studied. The evolution of the residual stress in AlN layers as a function of layer thickness is estimated by the X-ray diffraction technique. A mushroom-shaped AlN/ Si (111) MEMS resonator structure is designed. The effect of the

residual stress in the AlN films on the modal pattern, resonant frequency and quality factor of the resonator structure are studied and reported.

2 Experimental

Aluminium nitride thin films were deposited on silicon (111) substrate by DC magnetron reactive sputtering (India made: Excel Instruments) technique. In the magnetron sputtering Aluminium target was used with 99.9% purity. For reactive sputtering high-purity gases, Argon (Ar) and Nitrogen (N_2) gases were used for plasma creation and reactive gas, respectively. Si substrate was properly cleaned by RCA cleaning method which was explained in our previous report [35]. After cleaning the substrate, it was loaded in the sputtering chamber. The chamber pressure was first stabilized $\sim 10^{-6}$ Torr then Ar gas was inserted into the chamber. To remove the unintentional oxide on the target surface, the target was pre-sputtered around 15 min. For the wurtzite phase AlN thin film growth, the growth conditions were properly optimized and reported in our previous publication [37]. Three AlN thin film samples were grown at ~ 90 W DC power and Ar and N_2 mixture flow rate ~ 20sccm (10 sccm + 10 sccm) by varying the deposition time. To get < 001 > oriented AlN thin films on Si (111), the best-optimized temperature substrate ~ 500 °C was utilized. During the deposition, the substrate to target separation was kept ~ 6 cm. Three samples were grown by varying the deposition time from ~ 0.75 h, ~ 1 h and ~ 1.25 h, respectively, for this study. During the film deposition, a step was made on the substrate for thickness estimation. The thicknesses of the films were estimated by Stylus Surface Profiler (KLA-Tencor Alpha-Step D-500 stylus profiler).

AlN layers phase and crystalline identification and scan for residual stress were done by Grazing incidence X-ray diffraction (GIXRD) technique in thin film geometry using PANalytical X'Pert Pro MRD system. In the GIXRD technique incident angle of X-rays was kept constant around 2° from the sample surface and the detector was scanned (2θ angle) from 30° to 70°. Using this scan X-ray diffractogram were recorded for AlN layers. A parabolic mirror was used in the incident side in front of the X-ray source and a proportional counter detector was used on the diffracted side. For residual stress estimation of the AlN

layers, several XRD data were measured near 65.9° angle with the range of 5° by varying the tilt angle from 0° to 45°. Surfaces morphologies of the AlN layers were recorded using Zeiss make Field Emission Scanning Electron Microscope (FESEM) (Model: Supra 55).

3 Results and discussion

3.1 Structural characterization

The film thickness was measured by the depth profilometer. The thickness of the AlN layers is found to be 700 nm, 900 nm and 1200 nm for the film deposited in ~ 0.75 h, ~ 1 h and ~ 1.25 h, respectively. The X-ray diffraction pattern was recorded of AlN thin films from angle 30° to 70° and shown in Fig. 1. In the XRD plot, several intense peaks were observed at 33°, 35.9°, 38°, 49°, 59° and 65.9° diffracted angle. These peaks are very well matched with the polycrystalline wurtzite structure of AlN and showing the (100), (002), (101), (102), (110) and (103) crystallographic planes, respectively. The XRD peak position is very well matched with the standard JCPDS file (file no 08–0262). The observed intense peak of (002) planes near $\sim 35.9°$ in all samples represent the AlN films are preferred oriented along c-direction. As the thickness of the film increases, the relative intensity of (002) peak also increases. The film's orientation parameter (texture coefficient) for AlN samples along the (002) plane is estimated by the procedure mentioned in the earlier report [35]. The estimated texture
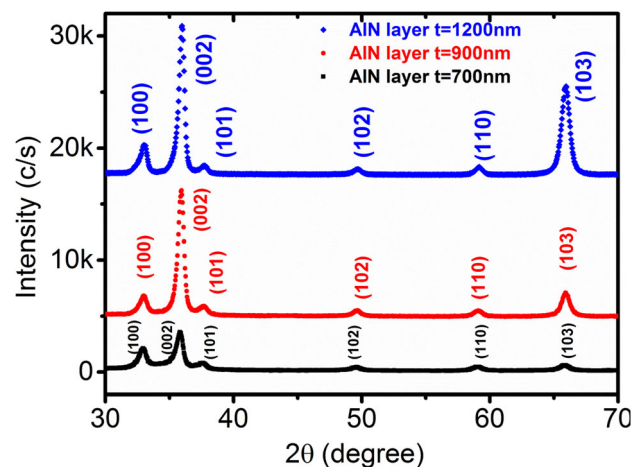

Fig. 1 X-ray diffraction pattern of the AlN layer on Si (111): thickness $\sim$ 700 nm, 900 nm, 1200 nm, respectively

coefficient of the AlN films is around 2.7, 3.2 and 3.6 for AlN layer with film thickness 700 nm, 900 nm and 1200 nm, respectively. The crystallite size of the films is calculated by Scherer equation ($D = 0.94*\lambda/\beta\cos(\theta)$) [35], β and θ represent the FWHM and Bragg's angle, respectively. The crystallite size of the films is found in the range ∼ 18–35 nm.

GIXRD technique is used to determine the strain value of thin film by recording the diffraction curve by varying the tilt value for a higher-order indexed plane. Subsequently, the residual stress of AlN layers on Si (111) substrate is estimated by the modified $\sin^2\psi$ method [35, 47]. For strain determination, the XRD measurement is recorded a high (2θ) angled plane by varying tilt angle (ψ) in GIXRD geometry. The strain in the (hkl) plane can be written as

$$\varepsilon = \frac{d\alpha\psi(hkl) - d_0(hkl)}{d_0(hkl)} \quad (1)$$

where $d\alpha\psi(hkl)$ and $d_0(hkl)$, represent the interplanar separation of the (hkl) plane in the presence and absence of residual stress. The residual stress (σ) generated in the AlN films can be extracted from the slope between ε and $\cos^2\alpha\sin^2\psi$ as written in Eq. (2) [47].

$$\varepsilon = \frac{1+v}{E}\sigma\left(\cos^2\alpha\sin^2\psi\right) + \frac{1+v}{E}\left(\sigma\sin^2\alpha\right) - \frac{2v}{E}\sigma \quad (2)$$

By combining Eqs. (1) and (2), strain (ε) is plotted with $\cos^2\alpha\sin^2\psi$ and it is found the plot is linear. In Eq. (2), E and v are young modulus and Poisson ratio, respectively. Here v and E are taken to be 0.236 and 322 GPa, respectively, for AlN material [48, 49]. Residual stress (σ) of the thin films samples are estimated from the gradient of $d\alpha\psi(hkl)$ and $\cos^2\alpha\sin^2\psi$ plot by Eq. (2). In the Eq. (2), ψ is the sample tilt angle from the sample surface which was provided to the goniometer stage during the X-ray diffraction experiments, and the angle (α) is equal to ($\theta-\gamma$), where γ is glancing incidence angle in XRD measurement.

The XRD peak around (2θ–65.9°) corresponding to the (103) plane is chosen for residual stress determination for AlN layers. Figure 2a–c shows the 2θ scan for (103) plane around ($2\theta \sim 65.9°$) by varying tilt (ψ) angle from 0° to 45° for AlN films grown on Si(111) substrate with the layer thicknesses around ∼ 700 nm, 900 nm, 1200 nm. In the plots, A-I corresponds to the XRD plot of varying the tilt angle (ψ) taken from
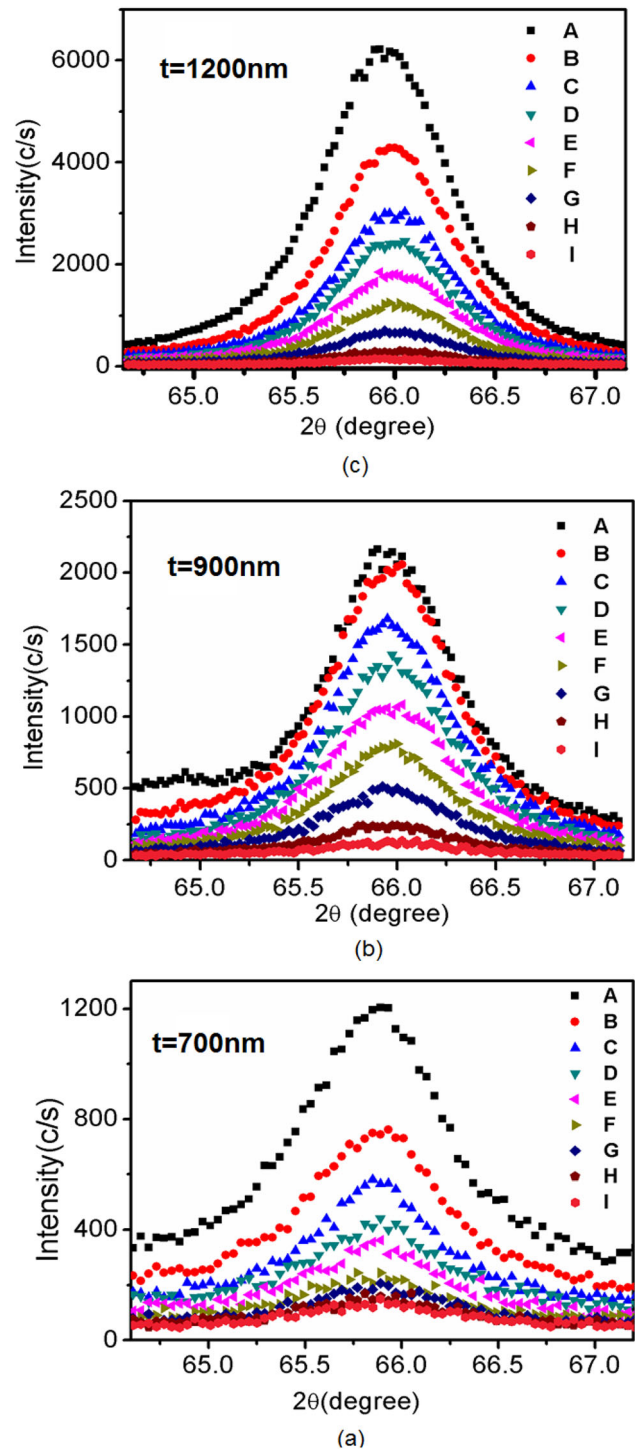

Fig. 2 Residual stress determination of the AlN films by recording 2θ scan of (103) plane AlN layers at different tilt angle ($\psi = 0$–45°) in GIXRD geometry: film thickness **a** 700 nm, **b** 900 nm and **c** 1200 nm. Plot **A** to **I** represents the XRD patterns at every 5° steps of the ψ

0° to 45° at an equal interval (around 5°) for the samples. Figure 2 indicates that as the tilt angles

increases, the XRD peak is shifted in the higher 2 theta angle side, implying the reducing the inter planner spacing. As a result, films are compressively strained.

For the residual stress (compressive) determination Fig. 3 is plotted using the Eqs. (1) and (2). Figure 3a–c shows the plot between d-spacing versus $\sin^2\psi \cos^2\alpha$ for (103) plane for the AlN layer of thickness 700 nm, 900 nm, 1200 nm, respectively. The extracted residual stress values for AlN layers were found to be compressive. The residual stress values of the AlN samples were found to be − 1050 MPa, − 500 MPa, and − 230 MPa for the 700 nm, 900 nm, 1200 nm thin films, respectively. The error value in the residual stress in the GIXRD measurement is also calculated. It depends on the value of the step size taken during 2 theta scan and the wavelength spread. The calculated error value (accuracy) is found to about ± 25 MPa. The in-plane lattice arrangement of Si (111) (in-plane lattice arrangement, i.e. hexagonal) and AlN film-oriented along c-direction (hexagonal in-plane atomic arrangement) is similar; therefore, the determined residual stress values are found to be lesser values as compared to other reports [35]. As the thickness and crystallite size of the films increases, the residual stress value decreases.

The AlN layers were grown on Si (111) substrate at same temperature 500 °C with similar conditions; therefore similar kind of substrate induced stress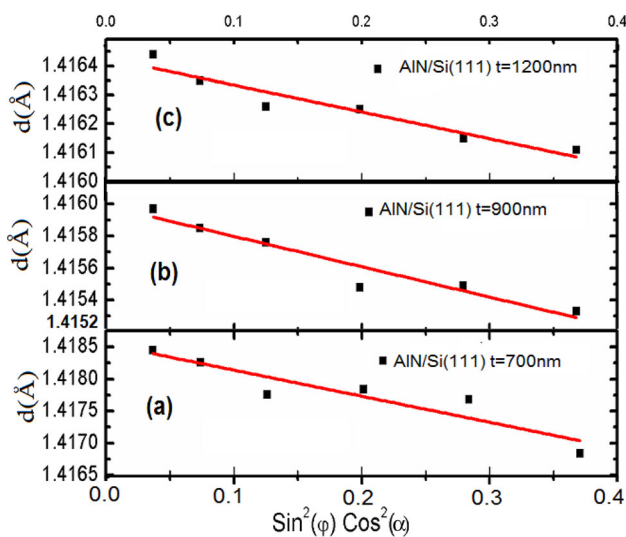 (or strain) is expected in all the samples. The GIXRD measurement was done at a constant grazing angle of 2°. So, the effect of substrate in the GIXRD measurement will be more prominent in the lower thickness sample (700 nm) as compared to higher thickness of AlN films of Si (111) substrate. This might be the one of the reasons for getting the slight difference in d values in 700-nm-thick AlN thin films. Moreover, the internal stress arises due to the presence of large number of grains/grain boundaries, defects and impurities also contributing in determining the resultant residual stress in the film. In lower thickness (700 nm), the smaller grain size and higher grain boundary density yielded higher resultant residual stress in the film. The gradual increase in grain size and hence lower grain boundary density with the increase in film thickness resulted steady decrease in the resultant residual stress in the AlN films. Thus, the d values as well as compressive stress in 700-nm-thin AlN layer is high as compared to other AlN thin layers, i.e. 900 nm and 1200 nm.

Figure 4a–c shows the FESEM images for AlN samples with layer thickness ∼ 700 nm, 900 nm, 1200 nm, respectively, using 200 KX magnification. The surface morphologies of the sample with layer thickness are different in terms of their grain size and grain boundaries. The mean grain size of the films with layer thickness ∼ 700 nm, 900 nm and 1200 nm are ∼ (15–20 nm), ∼ (20–25 nm) and ∼ (25–35 nm), respectively. At lower deposition growth time (duration) of AlN films showing the low grain size, as the growth time increases, the grain size also increases as shown in Fig. 4. The AlN layer thickness ∼ 700 nm, 900 nm films have shown uniform grains and larger grain boundary density (grain boundary perimeter span per unit surface area) as compared to the thicker film, (1200 nm) which shows the larger grain size and low grain boundary density as shown in Fig. 4. The measured grain size by SEM images is very well matched with the crystallite size determined by XRD.

The decrease in the residual stress in the AlN layers as the thickness of the films increase depends on the microstructure of the AlN films. As the thickness of the film increased large grain size and reduced grain boundaries (observed in SEM image) might be responsible to relax the residual stress in the AlN layer.
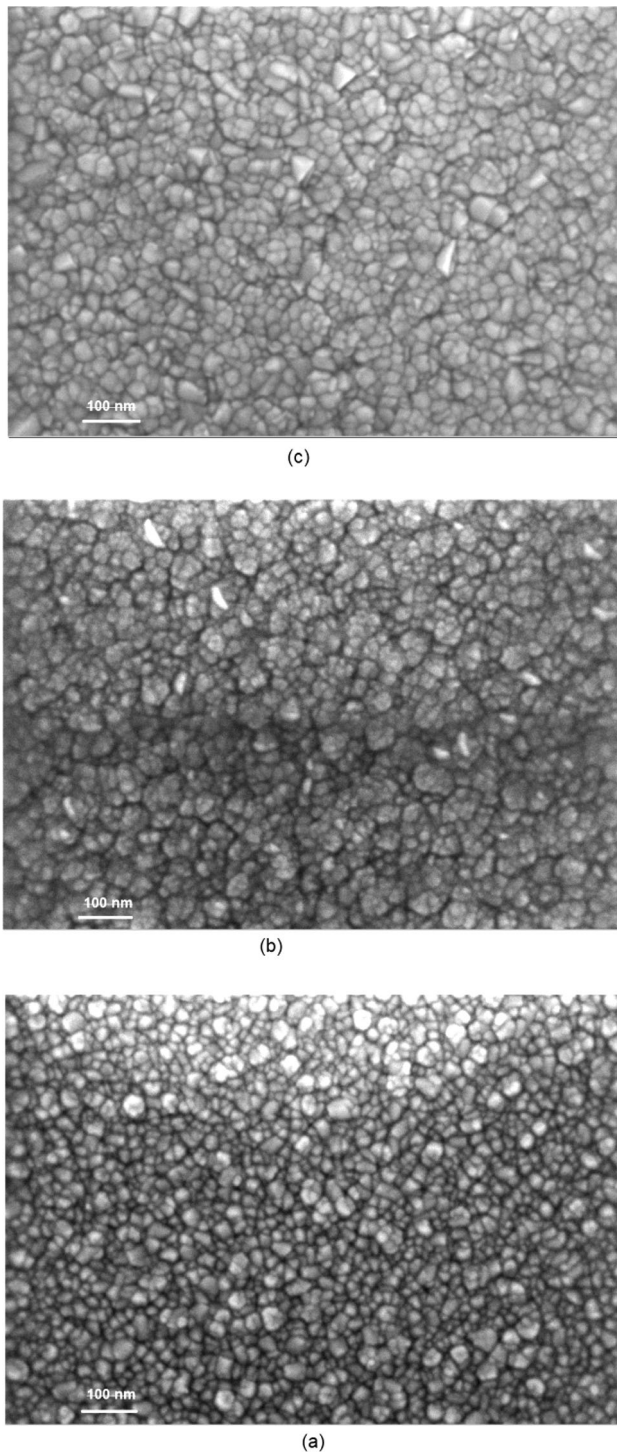

Fig. 3 The d-spacing versus $\cos^2\alpha\sin^2\psi$ plot of the AlN layers of thickness: (a) 700 nm, (b) 900 nm, and (c) 1200 nm for residual stress determination by X-ray diffraction

Fig. 4 Surface morphology (FESEM image) of the AlN thin films having a thickness of **a** 700 nm, **b** 900 nm, and **c** 1200 nm

3.2 Effect of residual stress in mushroom-shaped MEMS Resonator design

The deposited AlN layers are used in this study for the development of the piezoelectric MEMS resonator structure. A mushroom-shaped AlN-based resonator structure is designed, as shown in Fig. 5. The top AlN disc of the mushroom-shaped structure has a diameter of 500 μm, which is supported by a cylindrical post (diameter: 250 μm and height 400 μm) of bulk-micromachined silicon. The resonator structure can easily be fabricated using DRIE-assisted bulk micromachining process. The mushroom-shaped resonator structure will be helpful in generating different acoustic frequencies by easily varying the mode shapes of the piezoelectric AlN disc attached to the silicon post. The measured residual stresses (− 1050 MPa to − 230 MPa) in the sputtered AlN layers are added in the finite element simulation model of the resonator structure. The influence of the residual stress (σ_R) on the performance of the resonator structure is studied using Coventorware software. Figure 6 shows the initial deflection of the piezoelectric disc of the MEMS resonator at different residual stresses. The AlN disc is deformed in different shapes due to the different values of residual stresses in the AlN layers. The maximum simulated deflections in the AlN disc due to the residual stresses are 1.5 μm ($\sigma_R = -$ 1050 MPa), 0.18 μm ($\sigma_R = -$ 500 MPa), 0.055 μm ($\sigma_R = -$ 230 MPa).

Since the resonating frequencies and the mode shapes are very important in defining the resonator behaviour, the effect of the residual stresses (− 1030 MPa, − 500 MPa, and − 230 MPa) on the modal behaviour of the mushroom-shaped AlN
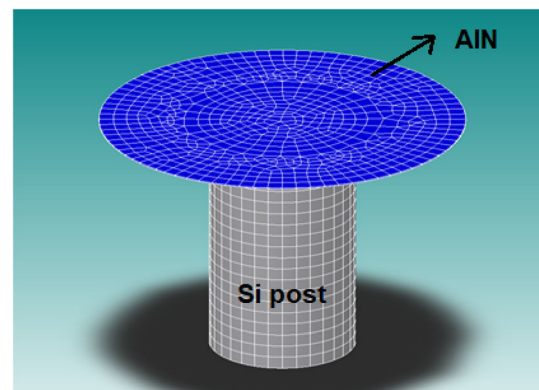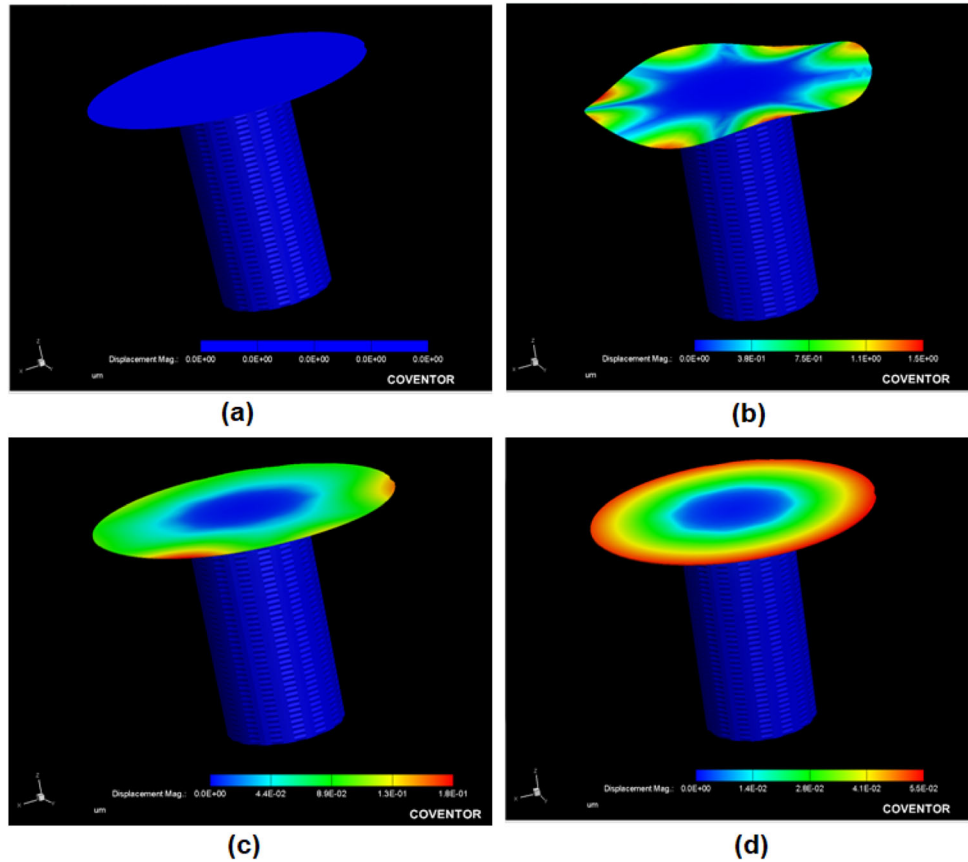

Fig. 5 Mushroom-shaped resonator structure design using AlN membrane

Fig. 6 Initial displacement in the resonator structure at **a** $\sigma_R = 0$; **b** $\sigma_R = -1050$ MPa; **c** $\sigma_R = -500$ MPa; and **d** $\sigma_R = -230$ MPa

(a)　(b)

(c)　(d)

MEMS resonator structure is studied. Figure 7 shows the first five modal patterns of the resonator structures having 700 nm, 900 nm and 1200-nm-thick AlN layers. In the absence of any residual stress, the resonator structures exhibited out of the plane (z-axis) primary vibration mode (denoted by f_1), as shown in Fig. 7a, c and e, respectively. The other four modes show higher-order harmonics of the resonator structure. The introduction of the residual stress in the resonator structure (via AlN layer growth), alters the shape of the primary mode (f_1) as shown in Fig. 7b, d, f, respectively. Higher-order harmonics of the MEMS structure also severely modified in the presence of the residual stresses.

The resonant frequency of the MEMS structure is found to be 235 kHz, 280 kHz and 344 kHz corresponding to the AlN film thickness 700 nm, 900 nm, 1200 nm as shown (by arrow mark) in Fig. 8a, c, e), respectively. Higher-order vibrational modes are shown complex deformation of the AlN membrane. In the presence of residual stress, several higher-order vibrational modes have now become the primary mode of vibration. The resonant frequency of

the MEMS structure is altered to 65 kHz, 75 kHz and 371 kHz corresponding to the residual stress of − 1050 MPa(thickness: 700 nm), − 500 MPa (thickness: 900 nm) and − 230 MPa (thickness: 1200 nm), respectively, as shown (by arrow mark) in Fig. 8b, d and f. Many of the initial modes are not energetically favourable due to the presence of residual stress, which modified the force-balance equations of vibrations. The detailed frequency response of the MEMS resonator in all the five modes shapes can also be observed in Fig. 8.

Since the resonant frequency of the MEMS structure is altered due to the residual stress, it is also bound to affect its quality factor. The quality factor (Q) is defined as

$$Q = \frac{f_0}{\Delta f} \tag{3}$$

where f_0 is the resonant frequency and Δf is the full width half maximum (FWHM) of the resonance intensity spectrum. In the absence of residual stress, the resonator exhibited FWHM (at the resonant peak) of 0.95 kHz (thickness: 700 nm), 1.23 kHz (thickness: 900 nm), and 1.43 kHz (thickness: 1200 nm). From
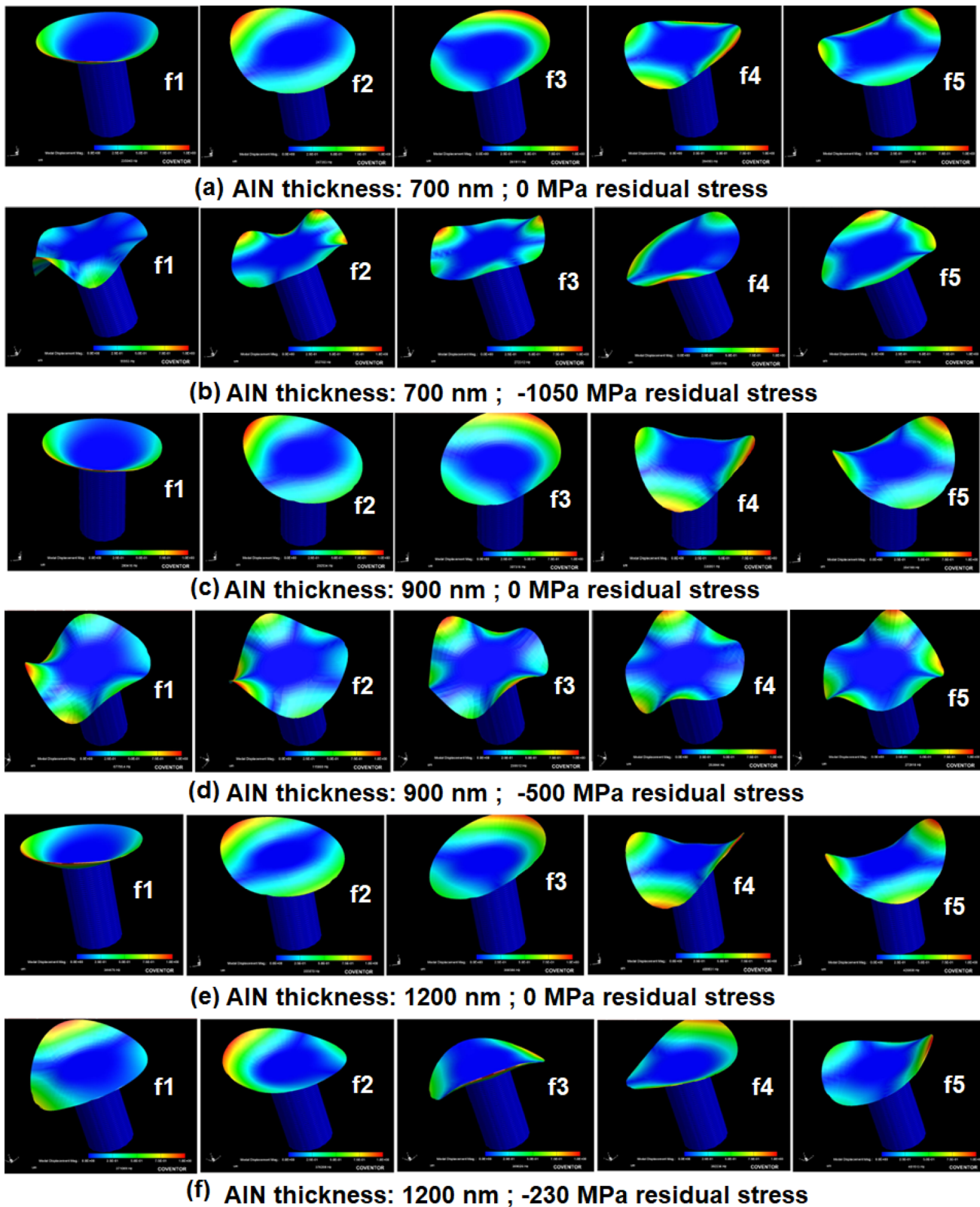
Fig. 7 Mode shapes of the MEMS AlN resonator structure: **a** AlN thickness: 700 nm; $\sigma_R = 0$ MPa; **b** AlN thickness: 700 nm; $\sigma_R = -$ 1050 MPa; **c** AlN thickness: 900 nm; $\sigma_R = 0$ MPa; **d** AlN thickness: 900 nm; $\sigma_R = -$ 500 MPa; **e** AlN thickness: 1200 nm; $\sigma_R = 0$ MPa; and **f** AlN thickness: 1200 nm; $\sigma_R = -$ 230 MPa

Fig. 8 Modal frequency response of the MEMS resonator structure: **a** AlN thickness: 700 nm; $\sigma_R = 0$ MPa; **b** AlN thickness: 700 nm; $\sigma_R = -1050$ MPa; **c** AlN thickness: 900 nm; $\sigma_R = 0$ MPa; **d** AlN thickness: 900 nm; $\sigma_R = -500$ MPa; **e** AlN thickness: 1200 nm; $\sigma_R = 0$ MPa; and **f** AlN thickness: 1200 nm; $\sigma_R = -230$ MPa
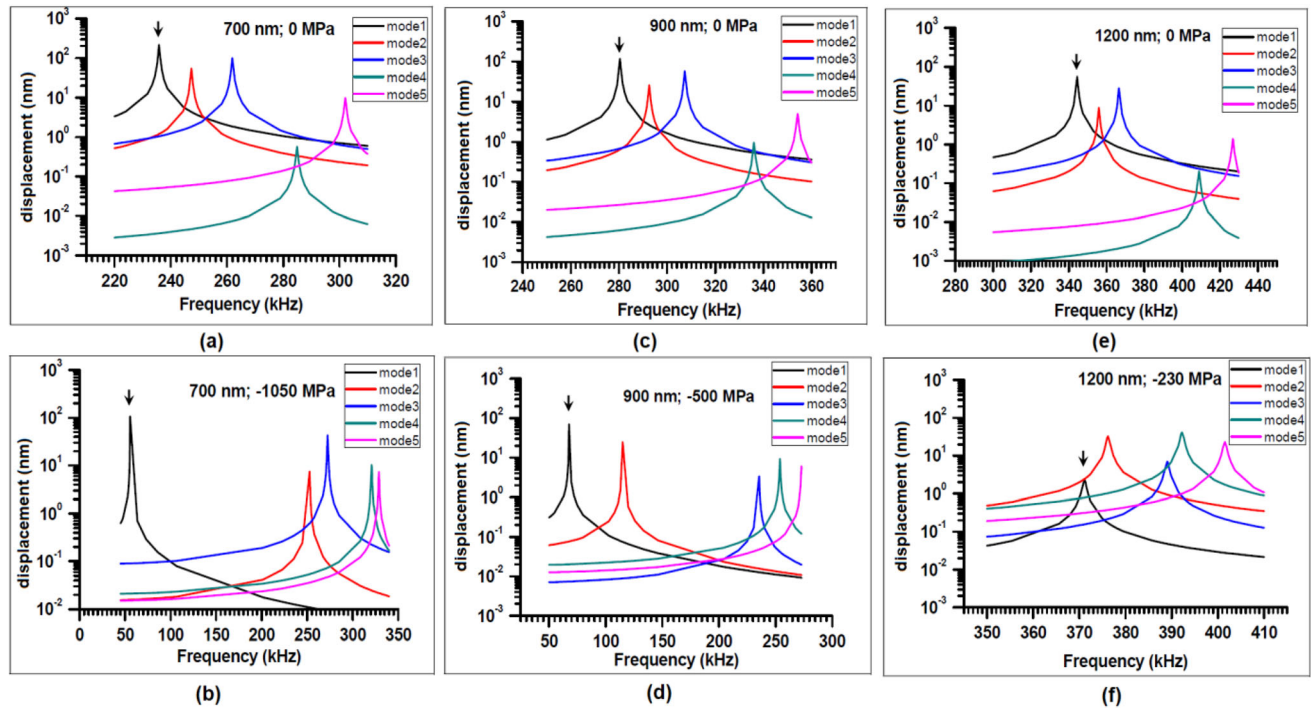
Eq. (1), the quality factor of the resonator is found to be 248, 227, 241 corresponding to the AlN film thickness of 700 nm, 900 nm, 1200 nm, respectively. The presence of residual stress, altered the FWHM values of the corresponding resonant peak to 2.31 kHz (−1050 MPa), 1.41 kHz (−500 MPa) and 1.42 kHz (−230 MPa), respectively. The Q value of the resonator structure is found to be 28, 53, and 261 corresponding to the residual stress of −1050 MPa, −500 MPa and −230 MPa, respectively. Thus, residual stress generated during the AlN film deposition severely altered the mode shapes, frequency response and quality factor of the AlN-based piezoelectric MEMS resonator structure.

According to the Rayleigh–Ritz principle, the resonant frequency of any multi degree of freedom vibrating body depends on its ratio of potential energy and kinetic energy [50, 51]. The residual stress changed the potential energy and stiffness of the of the MEMS structure. The presence of strain energy (due to the residual stress in the AlN films) modifies the modal shape as well as modal frequencies of the MEMS resonator structure. As a result of it the resonant frequency (1st mode of vibration) of the AlN-based mushroom-shaped resonator structure altered

from its original values. A closure looks at the modal shapes in the Fig. 7 of the resonator structure (with the residual stress) reveal that the resonant mode is no longer same as that was in absence of the residual stress.

With the gradual increase of residual stress in the MEMS structure induces gradual change in the modal frequency and its amplitude; finally, at appropriate level of stress it may vanish and higher-order mode start acts as the primary mode. Higher level of residual stresses in the 700 nm and 900-nm-thick AlN films yielded higher-order modes (7th or 8th mode) act as the primary resonant mode. In the 1200 nm thick AlN film-based resonator exhibited 3rd or 4th mode act as the primary mode in presence of 250 MPa compressive residual stress. Lower amplitude (compressed) of the resonant mode seems to be due to the influence of strain energy on the overall potential energy of the resonator structure.

4 Conclusions

The AlN-based MEMS resonators are developed in recent times for a wide variety of defence and civilian applications. But no reports are available on the detrimental effect of residual stress on AlN-based MEMS resonator design. This paper discussed growth and residual stress generated in the $< 001 >$ preferred oriented AlN/Si (111) using a reactive DC magnetron sputtering technique for MEMS resonator applications. Estimated residual stresses are $- 1050$ MPa, $- 500$ MPa, and $- 230$ MPa corresponding to the film thickness of 700 nm, 900 nm, and 1200 nm. The accuracy of residual stresses in the films is found about ± 25 MPa. The average grain sizes of the films are in the 15–40 nm range. A mushroom-shaped MEMS-based resonator structure has been designed. The effect of the residual stresses on the designed resonator structure is studied. The mode shapes, resonating frequencies, and the quality factor are severely affected due to the presence of the residual stresses. The resonant frequency of the MEMS structure for no residual stress is 235 kHz, 280 kHz, and 344 kHz corresponding to the AlN layer thickness of 700 nm, 900 nm, and 1200 nm, respectively. The resonant frequency of the structures is altered to 65 kHz, 75 kHz, and 371 kHz corresponding to the residual stress of $- 1050$ MPa (thickness: 700 nm), $- 500$ MPa (thickness: 900 nm) and $- 230$ MPa (thickness: 1200 nm), respectively. In absence of the residual stress, the quality factor of the resonator structures are 248, 227, 241 corresponding to the 700 nm, 900 nm, 1200-nm-thick AlN layers, respectively. In presence of the residual stress, the quality factor (Q value) of the resonator structures is decreased from 248 (thickness: 700 nm), 227 (thickness: 900 nm), 241 (thickness: 1200 nm) to 28, 53, and 261, respectively.

Acknowledgements

Funding

Data availability

The data that support the findings of this study will be available on request from the corresponding author.

Declarations

Conflict of interest I assure that this manuscript has not been submitted elsewhere for publication and all authors have been informed. There is not any conflict of interest regarding this manuscript.

References

1. M.Y. Chao, A. Ali, S. Ghosh, J. Lee, An aluminum nitride on silicon resonant MEMS accelerometer operating in ambient pressure, in IEEE 19th International Conference on Solid-State Sensors, Actuators, Microsystems (TRANSDUCERS) (2017), p. 607

2. Y.Q. Fu, J.K. Luo, N.T. Nguyen, A.J. Walton, A.J. Flewitt, X.T. Zu, Y. Li, G. McHale, A. Matthews, E. Iborra, H. Du, W.I. Milne, Advances in piezoelectric thin films for acoustic biosensors, acoustofluidics and lab-on-chip applications. Prog. Mater. Sci. **89**, 31 (2017)

3. N. Jaber, A. Ramini, Q. Hennawi, M.I. Younis, Wideband MEMS resonator using multifrequency excitation. Sens. Actuator A **242**, 140 (2016)

4. H. Lei, Q. Wen, F. Yu, D. Li, AlN film based piezoelectric large-aperture MEMS scanning micromirror integrated with angle sensors. J. Micromech. Microeng. **28**, 115012 (2018)

5. X. Li, Y. Huang, Y. Du, Z. Li, F. Bao, J. Bao, Study of a 10 MHz MEMS oscillator with a TPoS resonator. Sens. Actuator A **258**, 59 (2017)

6. H.P. Loebl, M. Klee, O. Wunnicke, R. Kiewitt, R. Dekker, E.V. Pelt, Piezoelectric AlN and PZT films for micro-electronic applications. IEEE Ultrason. Symp. **2**, 1031 (1999)

7. M. Marzencki, Y. Ammar, S. Basrour, Integrated power harvesting system including a MEMS generator and a power management circuit. Sens. Actuators A **145–146**, 363 (2008)

8. Y. Parmar, N. Gupta, V. Gond, S.S. Lamba, S.R.K. Vanjari, S. Dutta, K.K. Jain, D.K. Bhattacharya, Microsyst. Technol. **26**(3), 701 (2020)

9. G. Pfusterschmied, J. Toledo, M. Kucera, W. Steindl, S. Zemann, V.R. Díez, M. Schneider, A. Bittner, J.L.S. Rojas, U.

Schmid, Potential of piezoelectric MEMS resonators for grape must fermentation monitoring. Micromachines **8**, 200 (2017)

10. G. Pfusterschmied, F. Patocka, C. Weinmann, M. Schneider, D. Platz, U. Schmid, Responsivity and sensitivity of piezoelectric MEMS resonators athigher order modes in liquids. Sens. Actuator A **295**, 84 (2019)

11. S. Dutta, S.M. Imran, R. Pal, R.K. Bhan, Diffusion induced residual stress in comb-type microaccelerometer structure. J. Mater. Sci. **25**(9), 3828 (2014)

12. S. Dutta, A. Panchal, M. Kumar, R. Pal, R.K. Bhan, Effect of residual stress on modal patterns of MEMS vibratory gyroscope. AIP Conf. Proc. **1724**, 020103 (2016)

13. S. Dutta, P. Saxena, A. Panchal, R. Pal, K.K. Jain, D.K. Bhattacharya, Effect of vacuum packaging on bandwidth of push–pull type capacitive accelerometer structure. Microsyst. Technol. **24**, 4855 (2018)

14. N. Gupta, S. Dutta, A. Panchal, I. Yadav, S. Kumar, Y. Parmar, S.R.K. Vanjari, K.K. Jain, D.K. Bhattacharya, Design and fabrication of SOI technology-based MEMS differential capacitive accelerometer structure. J. Mater. Sci. **30**(16), 15705 (2019)

15. N. Gupta, A. Pandey, S.R.K. Vanjari, S. Dutta, Influence of residual stress on performance of AlN thin film based piezoelectric MEMS accelerometer structure. Microsyst. Technol. **25**, 3959–3967 (2019). https://doi.org/10.1007/s00542-019-04334-1

16. B. Kim, R.H. Olsson, K.E. Wojciechowski, AlN microresonator-based filters with multiple bandwidths at low intermediate frequencies. J. Microelectromech. Syst. **22**, 949–961 (2013)

17. A.L. Gesing, F.D.P. Alves, S. Paul, J.A. Cordioli, On the design of a MEMS piezoelectric accelerometer coupled to the middle ear as an implantable sensor for hearing devices. Sci. Rep. **8**, 3920 (2018)

18. M. Mehrpouya, H.C. Bidsorkhi, MEMS applications of NiTi based shape memory alloys: a review. Micro Nanosyst. **8**(2), 79 (2016)

19. U. Sharma, M. Kumar, R. Sharma, T. Saha, K.K. Jain, S. Dutta, E.K. Sharma, Fabrication process induced changes in scattering parameters of meander type RFMEMS shunt switch. Microsyst. Technol. **23**(12), 5561 (2017)

20. U. Sharma, S. Dutta, E.K. Sharma, Improved broadband (75–110 GHz) radio frequency characteristics of MEMS shunt switches on quartz substrate. Microsyst. Technol. **25**(3), 977 (2019)

21. H.C. Nathanson, W.E. Newell, R.A. Wickstrom, J.R. Davis, The resonant gate transistor. IEEE Trans. ED **14**(3), 117 (1967)

22. N. Alcheikh, S.A. Tella, M.I. Younis, An investigation into the mechanical behavior of multi-input and multi-output MEMS resonators. Sens. Actuators A **280**, 309 (2018)

23. F.H. Bao, J.F. Bao, J.E.Y. Lee, L.L. Bao, M.A. Khana, X. Zhoua, Q.D. Wu, T. Zhanga, X.S. Zhang, Quality factor improvement of piezoelectric MEMS resonator by the conjunction of frame structure and phononic crystals. Sens. Actuators A **297**, 111541 (2019)

24. F.H. Bao, Q.D. Wu, X. Zhou, T. Wua, X.Y. Li, J.F. Bao, High-Q multi-frequency ring-shaped piezoelectric MEMS resonators. Microelectronics **98**, 104733 (2020)

25. S. Ilyas, M.I. Younis, Resonator-based M/NEMS logic devices: review of recent advances. Sens. Actuators A **302**, 111821 (2020)

26. R.H. Olsson, K.E. Wojciechowski, M.S. Baker, M.R. Tuck, J.G. Fleming, Post-CMOS-compatible aluminum nitride resonant MEMS accelerometers. IEEE MEMS **18**(3), 671 (2009)

27. N. Sepulveda, D. Aslam, J.P. Sullivan, Polycrystalline diamond MEMS resonator technology for sensor applications. Diam. Relat. Mater. **15**, 398 (2006)

28. J. Toledo, V.R. Díez, M. Bertke, H.S. Wasisto, E. Peiner, J.L.S. Rojas, Piezoelectric MEMS resonators for cigarette particle detection. Micromachines **10**, 145 (2019)

29. C. Zhao, M.H. Montaseri, G.S. Wood, S.H. Pu, A.A. Seshiad, M. Krafte, A review on coupled MEMS resonators for sensing applications utilizing mode localization. Sens. Actuators A **249**, 93 (2016)

30. S.C. Ur, E.S. Kim, S.H. Yi, The Effects of residual stresses in the composite diaphragm on the performance of piezoelectric microspeakers. Electron Mater. Lett. **9**, 119 (2013)

31. J.C. Yu, C.B. Lan, System modeling of microaccelerometer using piezoelectric thin films. Sens. Actuators A **88**, 178 (2001)

32. H.G. Yu, L. Zou, K. Deng, R. Wolf, S. Tadigadapa, S.T. McKinstry, Lead zirconate titanate MEMS accelerometer using interdigitated electrodes. Sens. Actuators A **107**, 26 (2003)

33. E. Iborra, J. Olivares, M. Clement, L. Vergara, A.S. Hervas, J. Sangrador, Piezoelectric properties and residual stress of sputtered AlN thin films for MEMS applications. Sens. Actuators A **115**, 501 (2004)

34. J. Yang, M. Zhang, Y. He, Y. Su, G. Han, C. Si, J. Ning, F. Yang, X. Wang, A resonant z-axis aluminum nitride thin-film piezoelectric MEMS accelerometer. Micromachines **10**, 589 (2019)

35. A. Pandey, R. Prakash, S. Dutta, S. Dalal, R. Raman, A.K. Kapoor, D. Kaur, Growth and evaluation of residual stress of AlN films on Si (100) wafers. Mater. Sci. Semicond. Process. **52**, 16–23 (2016)

36. S. Pawar, K. Singh, S. Sharma, A. Pandey, S. Dutta, D. Kaur, Growth assessment and scrutinize dielectric reliability of c-axis oriented insulating AlN thin films in MIM structures for microelectronics applications. Mater. Chem. Phys. **219**, 74 (2018)

37. A. Pandey, R. Prakash, S. Dutta, S. Dalal, A. Kumar, A.K. Kapoor, D. Kaur, Growth and morphological evolution of c-axis oriented AlN films on Si (100) substrates by DC sputtering technique. AIP Conf. Proc. **1953**, 100028 (2018)

38. J.X. Zhang, J.X. Zhang, H. Cheng, Y.Z. Chen, A. Uddin, S. Yuan, S.J. Geng, S. Zhang, Growth of AlN films on Si (100) and Si (111) substrates by reactive magnetron sputtering. Surf. Coat. Technol. **198**, 68–73 (2005)

39. C. Caliendo, P. Imperaton, E. Cianci, Structural, morphological and acoustic properties of AlN thick films sputtered on Si(001) and Si(111) substrates at low temperature. Thin Solid Films **441**, 32–37 (2003)

40. H. Altuntas, C.O. Akgun, I. Donmez, N. Biyikli, Current transport mechanisms in plasma-enhanced atomic layer deposited AlN thin films. J. Appl. Phys. **117**, 155101 (2015)

41. Y. Feng, H. Wei, S. Yang, Z. Chen, L. Wang, S. Kong, G. Zhao, X. Liu, Competitive growth mechanisms of AlN on Si (111) by MOVPE. Sci. Rep. **4**, 06416 (2014)

42. S. Tanaka, R.S. Kern, J. Bentley, R.F. Davis, Defect formation during hetero-epitaxial growth of aluminum nitride thin films on 6h-silicon carbide by gas-source molecular beam epitaxy. Jpn. J. Appl. Phys. **35**, 1641 (1996)

43. K. Antonova, L. Duta, A. Szekeres, G.E. Stan, I.N. Mihailescu, M. Gartner, Influence of laser pulse frequency on the microstructure of aluminum nitride thin films synthesized by pulsed laser deposition. Appl. Surf. Sci. **394**, 197 (2017)

44. R.E. Sah, L. Kirste, M. Baeumler, P. Hiesinger, V. Cimalla, V. Lebedev, H. Baumann, H.E. Zschau, Residual stress stability in fiber textured stoichiometric AlN film grown using rf magnetron sputtering. J. Vac. Sci. Technol. A **28**, 394 (2010)

45. A. Pandey, S. Dutta, R. Prakash, R. Raman, A.K. Kapoor, D. Kaur, Growth and comparison of residual stress of AlN films on silicon (100), (110) and (111) substrates. J. Electron. Mater. **47**, 1405–1413 (2018)

46. Y. Ye, Z. Yi, M. Qin, Q. Huang, DRIE trenches and full-bridges design for sensitivity improvement of MEMS silicon thermal wind sensor, in IEEE 30th IntConf MEMS (2017), p. 985

47. C.H. Ma, J.H. Huang, H. Chen, Residual stress measurement in textured thin film by grazing-incidence X-ray diffraction. Thin Solid Films **418**, 73–78 (2002)

48. K. Kim, W.R.L. Lambrecht, B. Segall, Elastic constants and related properties of tetrahedrally bonded BN, AlN, GaN, and InN. Phys. Rev. B **53**, 16310 (1996)

49. R. Ruh, A. Zangvil, J. Barlowe, Elastic properties of SiC, AlN, and their solid-solution and particulate composites. Am. Ceram. Soc. Bull. **64**, 1368–1373 (1985)

50. M. Bao, *Analysis and Design Principles of MEMS Devices* (Elsevier Science Publication, Amsterdam, 2005).

51. A.W. Leissa, The historical bases of the Rayleigh and Ritz methods. J. Sound Vib. **287**(4–5), 961–978 (2005)